Available online at www.sciencedirect.com
ScienceDirect
Trans. Nonferrous Met. Soc. China 35(2025) 3306−3322
Transactions of Nonferrous Metals Society of China
www.tnmsc.cn

Creep behavior and microstructure evolution of TiAl alloys synergistically micro-alloyed with C and Y_2O_3 at different temperatures

Zhen-quan LIANG[1,2], Shu-long XIAO[1,2], Ye TIAN[1,2],
Yun-fei ZHENG[1,2], Ying-fei GUO[3], Li-juan XU[1,2], Xiang XUE[1,2], Jing TIAN[1,2]

1. National Key Laboratory for Precision Hot Processing of Metals,
Harbin Institute of Technology, Harbin 150001, China;
2. School of Materials Science and Engineering, Harbin Institute of Technology, Harbin 150001, China;
3. College of Materials and Metallurgy, Guizhou University, Guiyang 550025, China

Received 20 January 2024; accepted 24 June 2024

Abstract: The microstructure and creep behavior of C/Y_2O_3 synergistically micro-alloyed high-Al and low-Al TiAl alloys prepared by induction skull melting (ISM) technology were investigated by advanced electron microscopy. Microstructure analysis shows that Y_2O_3 particles are dispersed in both alloys; element C is dissolved in low-Al alloys as solid solution, while it exists as Ti_2AlC particles within lamellae in high-Al alloys. Additionally, high-density nanotwins are generated in high-Al alloys. Creep data show that C/Y_2O_3 micro-alloying significantly enhances creep resistance of TiAl alloys. This benefits from the dispersion strengthening of Y_2O_3 particles, precipitation hardening of dynamically precipitated Ti_3AlC particles and lamellar stabilization caused by dissolved C atoms or Ti_2AlC particles. This strategy causes a more significant improvement on creep resistance of high-Al TiAl alloys, which is attributed to extra twin strengthening effect. At 775−850 °C, these alloys fracture in mixed ductile−brittle mode, but the fracture characteristics change with the increase of temperature.

Key words: micro-alloyed TiAl alloy; creep behavior; twin strengthening; carbide precipitation; fracture characteristics

1 Introduction

Stimulated by the requirements of flexible mobility and higher efficiency of aircraft, the development of lighter and stronger high-temperature structural materials is imminent [1]. In recent years, TiAl-based alloys have attracted much attention, due to the benefits of low density, high specific strength, excellent oxidation resistance and the ability to replace heavier nickel-based super-alloys in the temperature range of 650−750 °C [2−4]. In order to improve the service temperature and comprehensive performance of TiAl alloys, the most common method is to tailor the microstructure through reasonable composition design.

The beneficial effects of solid solution elements such as Nb [5], Cr [6], V [7], Mo [8], Zr [9] and Fe [10] on the microstructure and mechanical properties have been studied in detail. These elements have a non-negligible effect on the phase constitution of TiAl alloys. In addition, the micro-alloying of non-metallic elements (B [11], C [12], Si [13], N [14]) and rare earth elements (Y [15], Ho [16], Gd [17], La [18]) has received much attention, and many new strengthening and toughening mechanisms triggered by these elements are still being reported. This may be related to

---

Corresponding author: Shu-long XIAO, Tel: +86-18745796616, E-mail: xiaoshulong@hit.edu.cn;
Li-juan XU, Tel: +86-18845618175, E-mail: xljuan@hit.edu.cn

https://doi.org/10.1016/S1003-6326(25)66882-8

flexible and diverse existence forms of these elements at high temperature. Taking element C as an example, when the C content is below the threshold, which depends on the alloy composition and microstructure, it is mainly dissolved in α_2 phase and plays a role of solid solution hardening [19]. When the C content is above the threshold, Ti_xAlC (x=2 or 3) carbides will precipitate and play a role of precipitation strengthening [20]. Besides, during long-term creep, new carbides may re-precipitate, further improving creep performance [21]. Recently, it has been found that twins are formed inside P-Ti_3AlC carbides in TiAl alloy during deformation, which makes it possible to achieve synergistic strengthening and toughening [22]. Such an interesting element deserves more research, but its benefits depend largely on the distribution and size of carbides. The coarse carbides are harmful to their strengthening effect. Therefore, it is necessary to adopt appropriate strategies to control the distribution and size of carbides.

In addition, recent studies are gradually focused on the synergistic micro-alloying, such as the development of Ti_2AlC/Mo_2B_5 [23], TiC/TiB_2 [24], Ti_5Si_3/Ti_2AlN [25] and other hybrid-reinforced structures. This strategy has achieved unexpected strengthening effects. Based on the previous research, this work intends to adopt a new alloy design strategy. First, changing the content of the main element Al to adjust the phase constitution. Then, introducing the element C and rare earth oxide Y_2O_3. Finally, applying long-term annealing to achieve in-situ precipitation of fine and dispersed carbides. It is hoped that the service performance of TiAl alloy, especially the creep resistance, can be improved by constructing a hybrid-reinforced structure.

As a hot-end structural component, sufficient creep resistance is one of the important indicators to determine whether TiAl alloys can serve for a long time at high temperature. There are many factors affecting creep performance, including internal alloy composition and microstructure characteristics [26], as well as external stress and temperature conditions [27,28]. Among them, the influence of temperature is inevitable. In aero-engines, the operating temperature at different parts is different, which is bound to lead to different creep strains and creep rates during effective service life [29]. From the perspective of microscopic creep mechanism, the change of temperature will directly cause the substructure evolution, which greatly affects the service stability. GUO et al [27] found that there is a critical temperature range during creep of TiAl alloy. Below this temperature, the deformation of α_2 lamellae is provided by $\boldsymbol{a}$ dislocations, while it is provided by $2\boldsymbol{c}+\boldsymbol{a}$ dislocations and larger creep strain occurs above this temperature. Moreover, it has been reported that the increase of temperature will promote the occurrence of the dynamic recrystallization during creep, which significantly accelerates the creep rate [30]. Hence, it is of great significance to explore the creep behavior at different temperatures, including macroscopic characteristics and microscopic mechanisms.

In this work, in order to improve the creep resistance of TiAl alloys, the synergistic micro-alloying strategy was applied on low-Al and high-Al TiAl alloys, respectively. The microstructure characteristics were characterized in detail by advanced electron microscopy techniques. The creep behavior at different temperatures was elucidated, including the fracture mechanism and phase precipitation mechanism. Meanwhile, multiple creep strengthening mechanisms were revealed. This study is expected to provide a valuable theoretical basis for the development of creep-resistant TiAl alloys and the design of service stability.

2 Experimental

2.1 Material preparation

In this study, two low-Al and two high-Al TiAl alloys were prepared by vacuum induction skull melting (ISM) technology in argon atmosphere. The nominal compositions (in at.%) of these four TiAl alloys are Ti−43Al−6Nb−1Cr−1.5V, Ti−43Al−6Nb−1Cr−1.5V−0.5C−$0.05Y_2O_3$, Ti−46Al−6Nb−1Cr−1.5V and Ti−46Al−6Nb−1Cr−1.5V−0.5C−$0.05Y_2O_3$, respectively. For ease of description, they are called T43, $T43^+$, T46 and $T46^+$ alloys. Raw materials used in this study included Ti bar (99.9 wt.%), pure Al (99.9 wt.%), pure Cr (99.9 wt.%), Al−V alloys (56.3 wt.% V), Al−Nb alloys (52.4 wt.% Nb), nano Y_2O_3 powders (99.9 wt.%) and pure graphite powders (99.9 wt.%). In order to ensure the uniform distribution of Y_2O_3

particles, nano Y_2O_3 powders were wrapped in aluminum foil and added into melt in the form of a block through a secondary hopper after other raw materials were completely melted. By adjusting the power, Y_2O_3 powders fell on the stable melt surface and sunk into the melt, rather than adhering to the crucible wall. More importantly, the melt was subjected to electromagnetic stirring for about 10 min to ensure the uniformity of Y_2O_3 particles. Then, the melt was poured into the preheated steel mold, and finally four ingots with a size of d50 mm × 100 mm were obtained. Subsequently, the ingots were subjected to long-term annealing at 950 °C for 36 h.

2.2 Creep test and microstructure characterization

The tensile creep tests were conducted on the RDL100 creep testing machine at 775−850 °C under 300 MPa until fracture. Creep specimens with the gauge size of 10 mm × 5 mm × 2 mm were obtained by electric discharge machining (EDM) method. In order to maintain the temperature uniformity during creep test, it is necessary to hold for 30 min at the test temperature before applying the creep load. Three thermocouples at different positions were used to ensure that the temperature fluctuation range is within ±1 °C. During tensile creep, the upper die was fixed, and the lower die moved down. The tensile creep strain (ε) was obtained by real-time displacement measurement of the lower die. Based on the equation of $\varepsilon=\Delta l/l$ (where Δl and l are the displacement of the lower die and the initial gauge length of the specimen, respectively), the tensile creep strain could be calculated.

The initial microstructure was characterized by X-ray diffraction with Cu K_α radiation (XRD), scanning electron microscopy (SEM) and transmission electron microscopy (TEM). After creep, the deformed microstructure characteristics and fracture surface morphology were observed by SEM in backscattered electron (BSE) mode and secondary electron (SE) mode, respectively. The TEM and high-resolution transmission electron microscopy (HRTEM) were used to detect the details of twins and precipitates. Samples for XRD and SEM analysis were prepared by standard metallographic techniques. The TEM samples were prepared by twin-jet electropolishing at 25 V and −30 °C in the solution consisting of 60 vol.% CH_3OH, 30 vol.% $CH_3(CH_2)_3OH$ and 10 vol.% $HClO_4$.

3 Results and discussion

3.1 Initial microstructure

Figure 1 shows the initial microstructure characteristics of four investigated alloys. It can be seen from the X-ray diffraction patterns in Fig. 1(a) that both T43 and T46 alloys are composed of γ, α_2 and $B2$ phases. Both alloys are characterized by the major α_2/γ lamellar colony and minor blocky $B2$ phase and γ phase, as shown in Figs. 1(b, c). They exhibit nearly lamellar structure. In contrast, the content of blocky $B2$ phase in T46 alloy is significantly lower than that in T43 alloy. After introducing trace C and Y_2O_3, the phase constitution of both alloys does not change obviously, which still consists of γ, α_2 and $B2$ phases, as verified in Fig. 1(a). In Figs. 1(d, h), bright white particles are dispersed in $T43^+$ and $T46^+$ alloy, which are confirmed as Y_2O_3 particles by the composition analysis results in Fig. 1(e). Due to the low content, they cannot be detected by XRD. In particular, there are the characteristic diffraction peaks of Ti_2AlC in the X-ray diffraction spectra of $T46^+$ alloy, but not in $T43^+$ alloy, as shown in Fig. 1(a). It can be found in Figs. 1(f, i) that there are uniform fine white particles in α_2/γ lamellae of $T46^+$ alloy, but not in $T43^+$ alloy. Through further TEM observation and the selected area electron diffraction (SAED) technique, it can be confirmed that white particles in lamellae of $T46^+$ alloy are Ti_2AlC carbides with an average size of 349.2 nm. In addition, abundant nanotwins are formed in the initial microstructure of $T46^+$ alloy, as shown in Figs. 1(k−m). The generation of these nanotwins has a positive effect on the creep resistance of $T46^+$ alloy.

3.2 Creep curves at different temperatures

Figure 2 shows the creep strain−time curves of four investigated alloys at 775−850 °C. With the extension of creep time, the creep strain increases nonlinearly. Two facts can be concluded from Fig. 2. On the one hand, the creep resistance of TiAl alloys is extremely sensitive to the alloy composition. When the Al content is increased from 43 to 46 at.%, the creep life is effectively prolonged, as shown in Figs. 2(a, c). After introducing trace C and Y_2O_3, the creep life is also significantly extended,

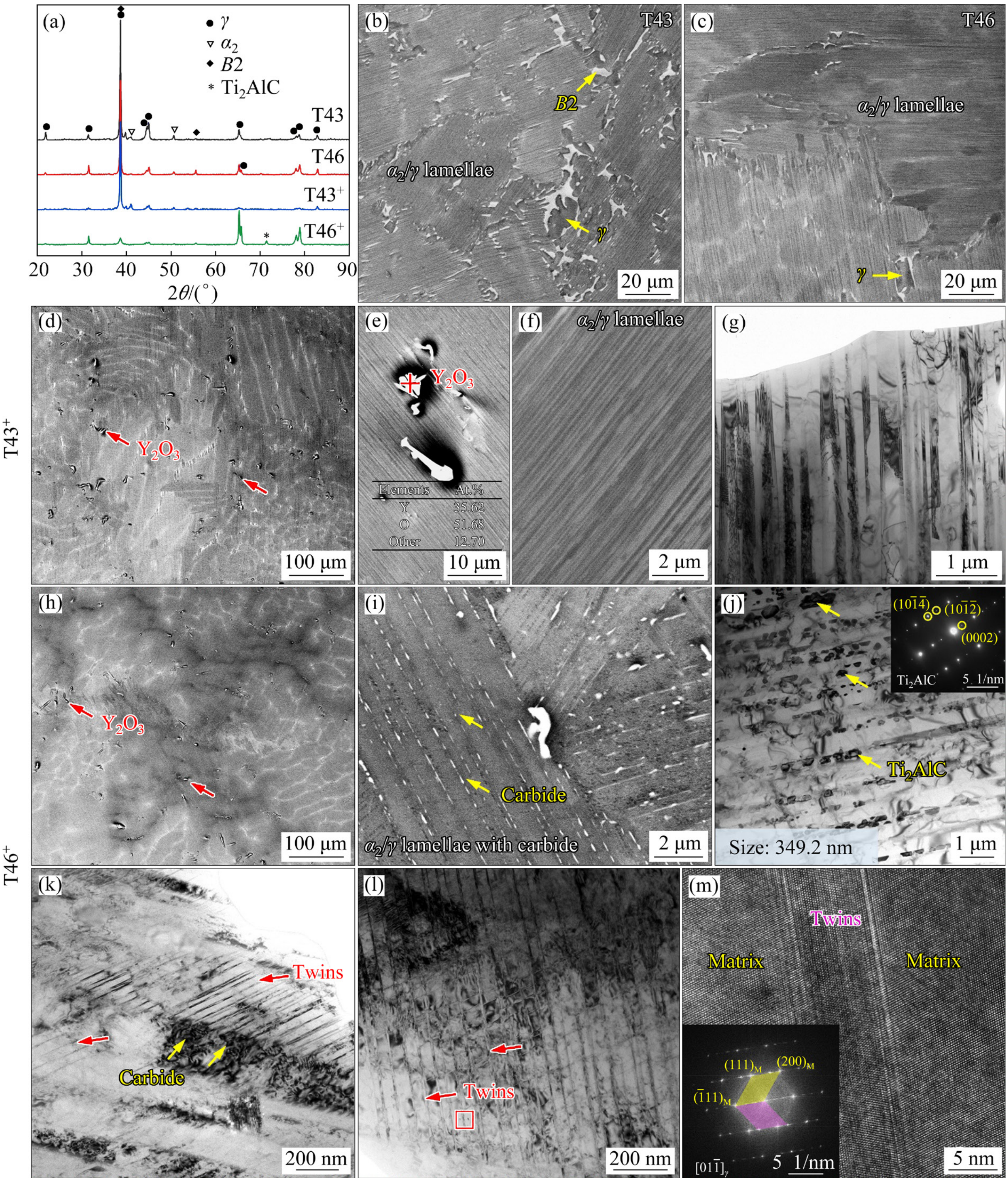

Fig. 1 Initial microstructures of four investigated alloys: (a) X-ray diffraction patterns; (b) SEM-BSE image of initial microstructure of T43 alloy; (c) SEM-BSE image of initial microstructure of T46 alloy; (d−g) SEM-BSE and TEM images of initial microstructure of T43$^+$ alloy; (h−l) SEM-BSE and TEM images of initial microstructure of T46$^+$ alloy; (m) HRTEM image of region enclosed by red box marked in (l)

and the creep strain is reduced. On the other hand, the tensile creep behavior of four alloys shows a strong dependence on temperature, which is manifested in the fact that the creep life decreases sharply with the increase of temperature. From 775 to 850 °C, the creep life of T43, T43$^+$, T46 and T46$^+$ alloys is shortened by 89.6%, 90.6%, 94.6% and 91.2%, respectively. This also strongly indicates that the creep resistance of TiAl alloy is a key factor to determine its service temperature limit.

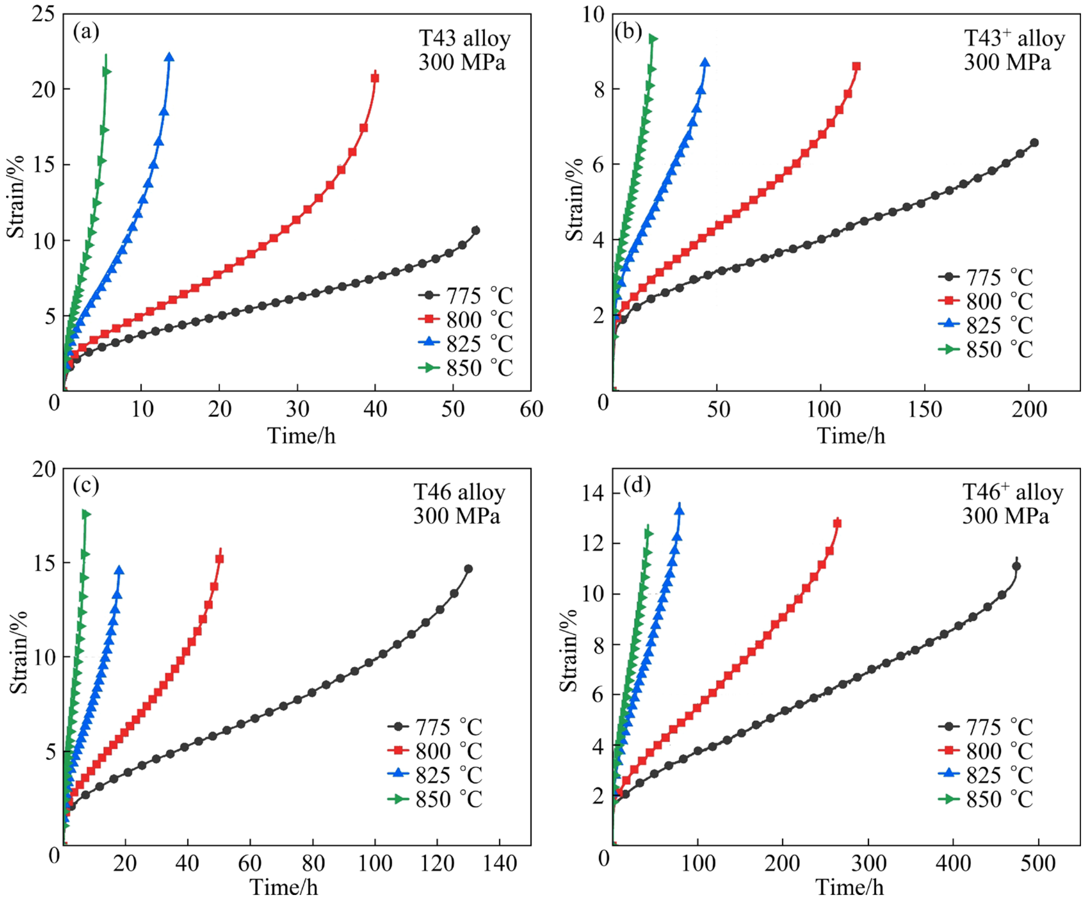

Fig. 2 Creep strain−time curves of four investigated alloys at 775−850 °C: (a) T43 alloy; (b) T43$^+$ alloy; (c) T46 alloy; (d) T46$^+$ alloy

In order to study the effect of temperature on the tensile creep behavior of four alloys, it is necessary to establish the creep kinetics based on the dependence of the minimum creep rate on temperature. In general, the minimum creep rate ($\dot{\varepsilon}_{\mathrm{m}}$) and the thermodynamic temperature (T) follow the Norton−Bailey power-law:

$$\dot{\varepsilon}_{\mathrm{m}}=A\sigma^{n}\exp\left(-\frac{Q_{\mathrm{C}}}{RT}\right) \tag{1}$$

where A is a material constant, σ is the creep stress, n is the stress exponent, R is the molar gas constant (8.314 J/(mol·K)), and Q_{C} is the apparent activation energy. Under a constant stress level, Q_{C} can be calculated by Eq. (2):

$$Q_{\mathrm{C}}=-R\left[\frac{\partial \ln \dot{\varepsilon}_{\mathrm{m}}}{\partial(1/T)}\right]_{\sigma=\mathrm{const}} \tag{2}$$

Figure 3 depicts the relationship between the minimum creep rate and the reciprocal of temperature. The creep activation energy values of T43 and T46 alloys are 383.519 and 408.024 kJ/mol at 775−850 °C, respectively, which are basically consistent with the self-diffusion activation energy (395 kJ/mol) of Al in α_2 phase [31]. After introducing C and Y_2O_3, the creep activation energy values of T43$^+$ and T46$^+$ alloys are reduced to 341.191 and 354.335 kJ/mol, respectively, which are comparable to the self-diffusion activation energy (358 kJ/mol) of Al in γ phase [32,33].

The creep activation energy refers to the thermal activation energy that controls the steady-state creep rate. For T43 and T46 alloys, γ phase and α_2 phase are the main constituent phases, and α_2 phase is more difficult to deform due to fewer independent slip systems. In this case, the dislocation motion and diffusion process in α_2 phase become the creep rate control mechanism. Therefore, the creep activation energy strongly depends on the energy required for the relevant physical processes in α_2 phase, such as the self-diffusion of Al. WANG et al [34] found that when the main dislocation slip systems in α_2 phase are activated, the creep activation energy increases accordingly and creep rate is accelerated. After introducing C and Y_2O_3, α_2 phase of T43$^+$ and T46$^+$ alloys is further hardened by solid solution and precipitation effects, and hardly participates in creep deformation. In this case, γ phase becomes the main contributor of creep deformation. Therefore, the element diffusion in γ phase dominates the creep rate. In contrast, the self-diffusion activation energy of Al in γ phase is lower than that in α_2 phase, which leads to a lower creep activation energy in T43$^+$ and T46$^+$ alloys. In view of the above analysis, the creep process of four alloys is inseparable from element diffusion. The temperature is an important factor determining the diffusion rate, and thus, the creep behavior of four alloys is obviously dependent on temperature.

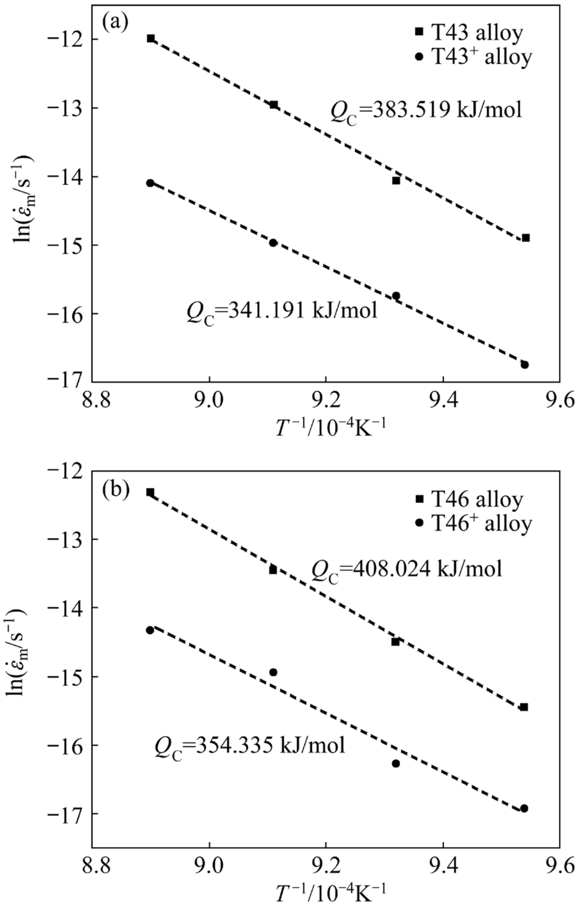

Fig. 3 Temperature dependence of minimum creep rate: (a) T43 and T43$^+$ alloys; (b) T46 and T46$^+$ alloys

3.3 Creep fracture behavior

Figure 4 shows the fracture surface morphology of T43 and T43$^+$ alloys after creep at different temperatures. There are obvious evidences of interlamellar fracture characterized by cleavage planes and translamellar (TL) fracture, which means the occurrence of brittle fracture, (Figs. 4(a−h)). Meanwhile, there are also numerous dimples on the fracture surface, which is a typical feature of ductile fracture (Figs. 4(a_1−h_1)). Therefore, the creep fracture mode of both alloys in the range of 775−850 °C is mixed ductile−brittle mode. In contrast, the dimples in T43 alloy are deeper and the tearing edges are clearly visible, while the dimples in T43$^+$ alloy are less obvious because they are covered by oxides. This is mainly because the crack propagation rate of T43$^+$ alloy is slow, so that the dimples formed before crack growth are severely oxidized. In addition, at the same creep temperature, the proportion of cleavage plane in T43$^+$ alloy is lower than that in T43 alloy. It is well known that cracks tend to propagate along the lamellar interface. In this case, abundant cleavage planes are formed. However, for T43$^+$ alloy, dissolved C atoms tend to be segregated at interlamellar locations [35], which slows down the diffusion process and dislocation motion at the lamellar interface. In this case, the crack propagation along the lamellar interface is more difficult, so the fracture surface exhibits fewer cleavage planes.

Similarly, in T46$^+$ alloy, Ti_2AlC carbides precipitate in the lamellae, which hinders the crack propagation along the lamellar interface, so cleavage plane characteristics in T46$^+$ alloy are fewer than those in T46 alloy (Fig. 5). It can be found that T46 and T46$^+$ alloys also fracture in mixed ductile−brittle mode. There is a common feature in four alloys: with the increase of creep temperature, the proportion of translamellar fracture in the brittle fracture characteristics increases, while that of interlamellar fracture decreases. This is related to the nucleation position of creep voids at different temperatures.

Figure 6 shows the deformed microstructure near the creep fracture of four alloys in the range of 775−850 °C. At 775 °C, in addition to the generation of main cracks, a small number of secondary cracks also appear, as indicated by the yellow arrows in Figs. 6(a, e, i, m). During the propagation of main cracks, the crack tip meets with different types of interfaces, including lamellar interface, $B2/\gamma$ phase interface, lamellar colony boundary, etc., due to the microstructure inhomogeneity and the diversity of the constituent

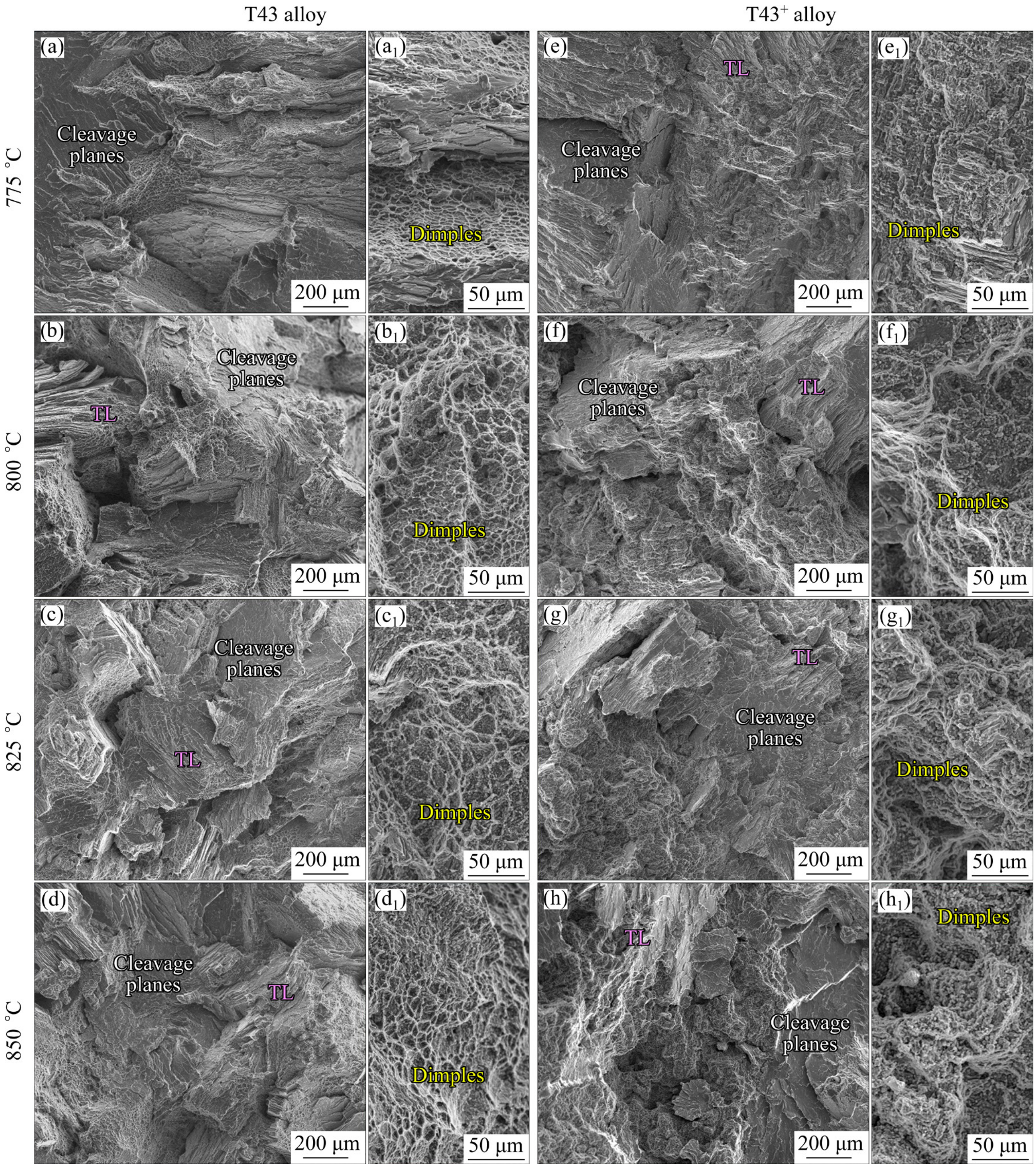

Fig. 4 Tensile creep fracture surface morphologies of T43 and T43$^+$ alloys at different temperatures

phase of four alloys. These interfaces have different resistance to crack propagation [36]. In this case, a part of the main crack tip can easily change the original propagation direction and deflect to form a new secondary crack. When the creep temperature rises to 800 °C, the number of secondary cracks gradually increases (Figs. 6(b, f, j, n)). As creep temperature further increases to 850 °C, another type of secondary crack gradually appears in four alloys. These secondary cracks do not originate from the main crack, but are formed by nucleation, growth and merging of voids at other locations, as indicated by the red arrows in Figs. 6(d, h, l, p). At higher temperatures, voids are easier to nucleate, which promotes the formation of more secondary cracks and accelerates creep fracture. In addition, compared with T43 and T46 alloys, T43$^+$ and T46$^+$ alloys containing C/Ti_2AlC and Y_2O_3 have fewer and shorter secondary cracks, exhibiting higher crack resistance.

Both the increase in the proportion of the translamellar fracture and the formation of secondary cracks with the increase of temperature may be related to the nucleation of creep voids.

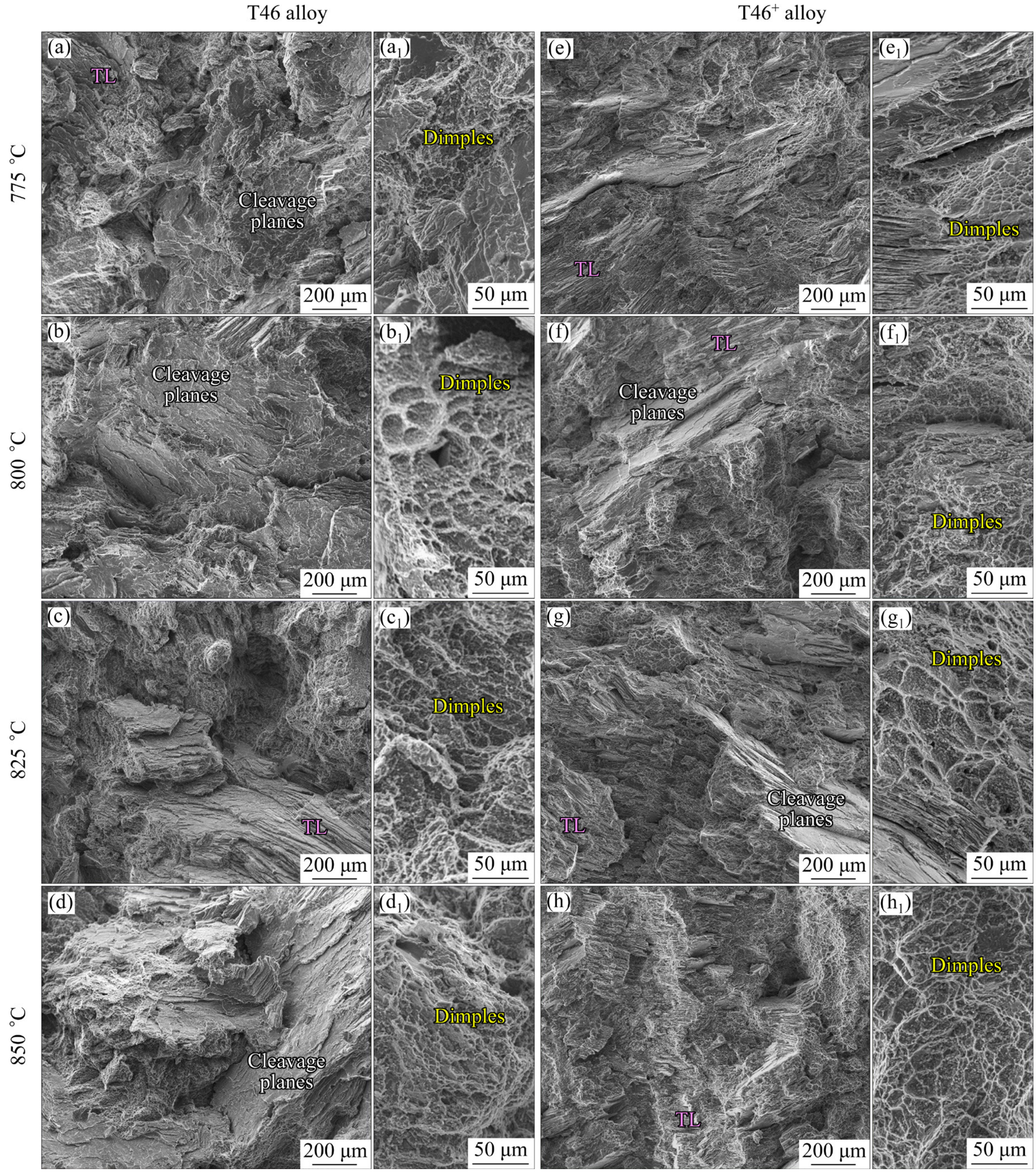

Fig. 5 Tensile creep fracture surface morphologies of T46 and T46$^+$ alloys at different temperatures

Therefore, the nucleation positions of creep voids at different temperatures are specially observed, as shown in Fig. 7. Obviously, in four alloys, creep voids tend to nucleate at the $B2/\gamma$ phase interface and $B2$/lamellar colony boundary, but the situation is slightly different with the change of temperature. At a lower temperature (775 °C), creep voids are mainly formed at the $B2/\gamma$ phase interface at the lamellar colony boundaries (Figs. 7(a, e, i, m)). As the temperature increases, in addition to the lamellar colony boundaries, more voids can also generate at the $B2/\gamma$ interface inside the lamellar colony. On the one hand, at higher creep temperatures, the increase in the void nucleation number and position creates conditions for the formation of more secondary cracks, accelerating fracture. On the other hand, at higher temperatures, voids nucleate and grow directly inside the lamellar colony, which further facilitates the outward propagation of cracks from the interior of lamellar

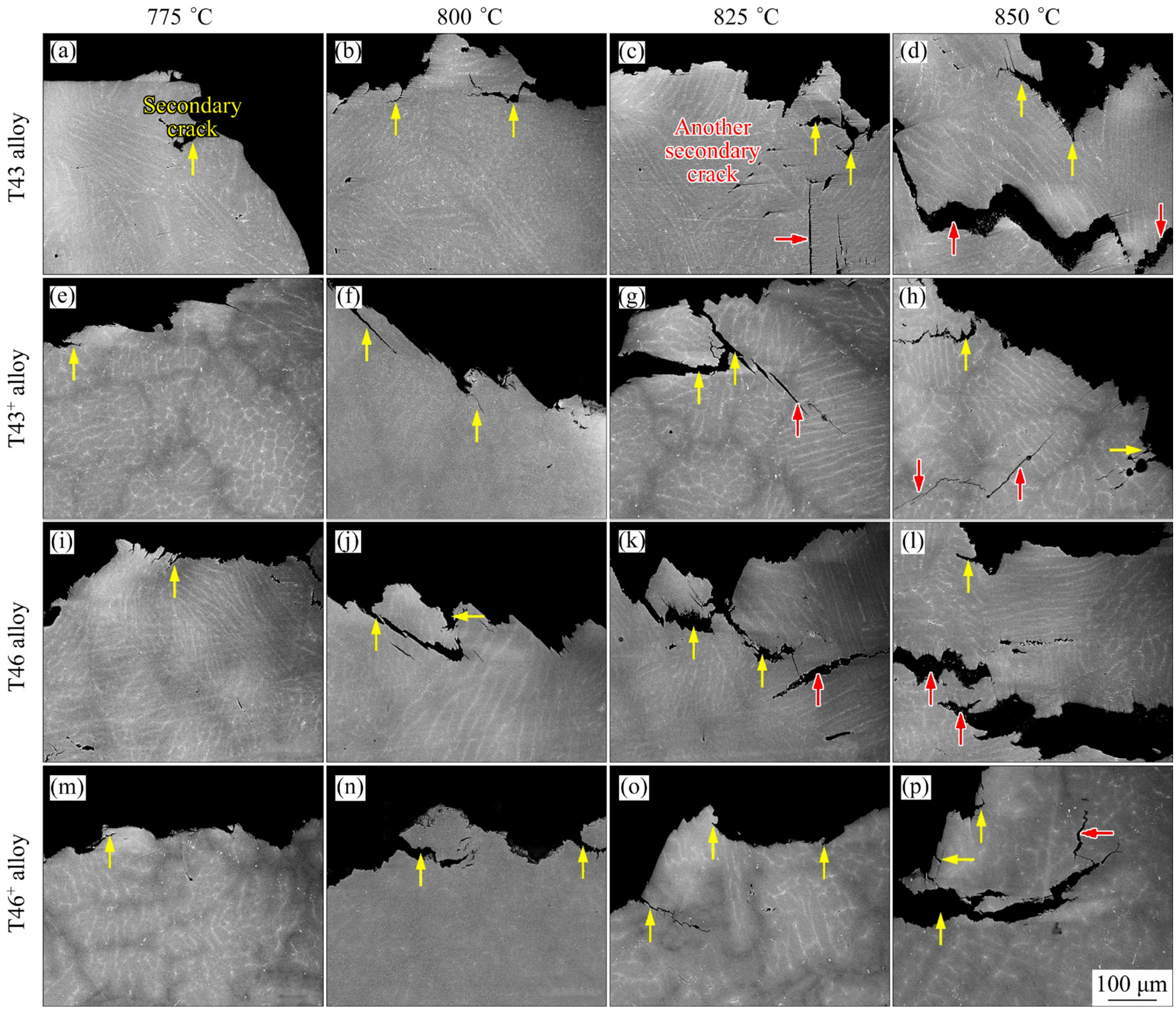

Fig. 6 Deformed microstructures near fracture of four investigated alloys at different temperatures

colony in the translamellar form. In addition, it can be concluded that introducing C and Y_2O_3 has no effect on the nucleation of creep voids.

3.4 Multiple creep strengthening mechanisms

It can be clearly seen in Fig. 2 that the creep resistance of both T43 alloy and T46 alloy is significantly enhanced after introducing C and Y_2O_3. The average increase of creep life of T43 alloy is about 237.85% in the temperature range of 775−850 °C, while that of T46 alloy is about 379.43%. This means that this strengthening strategy shows greater potential in high-Al TiAl alloys. More importantly, the creep resistance of T46$^+$ alloy is stronger than that of T43$^+$ alloy. The creep life of T46$^+$ alloy in the range of 775−850 °C is about 113.68% longer than that of T43$^+$ alloy. The average increase of creep life caused by the increase of Al content is about 58.08%. This implies that there are extra strengthening effects to contribute to the remaining increase of 55.60%. Therefore, it is necessary to reveal the multiple creep strengthening mechanisms.

3.4.1 Role of Y_2O_3 particles

As shown in Figs. 1(d, h), a large number of Y_2O_3 particles are dispersed in T43$^+$ and T46$^+$ alloys. Previous studies have reported that Y_2O_3 particles can play a key strengthening role in the tensile deformation of TiAl alloys at room temperature and high temperature [37,38]. In order to verify whether Y_2O_3 particles have a strengthening effect during creep, a detailed analysis was performed using TEM and SEM, as shown in Fig. 8. In the high-angle annular dark field (HAADF) image in Fig. 8(a), Y_2O_3 particles exhibit a bright white contrast due to higher atomic number. The composition analysis results in Fig. 8(a) and the SAED pattern in Fig. 8(c) confirm that these

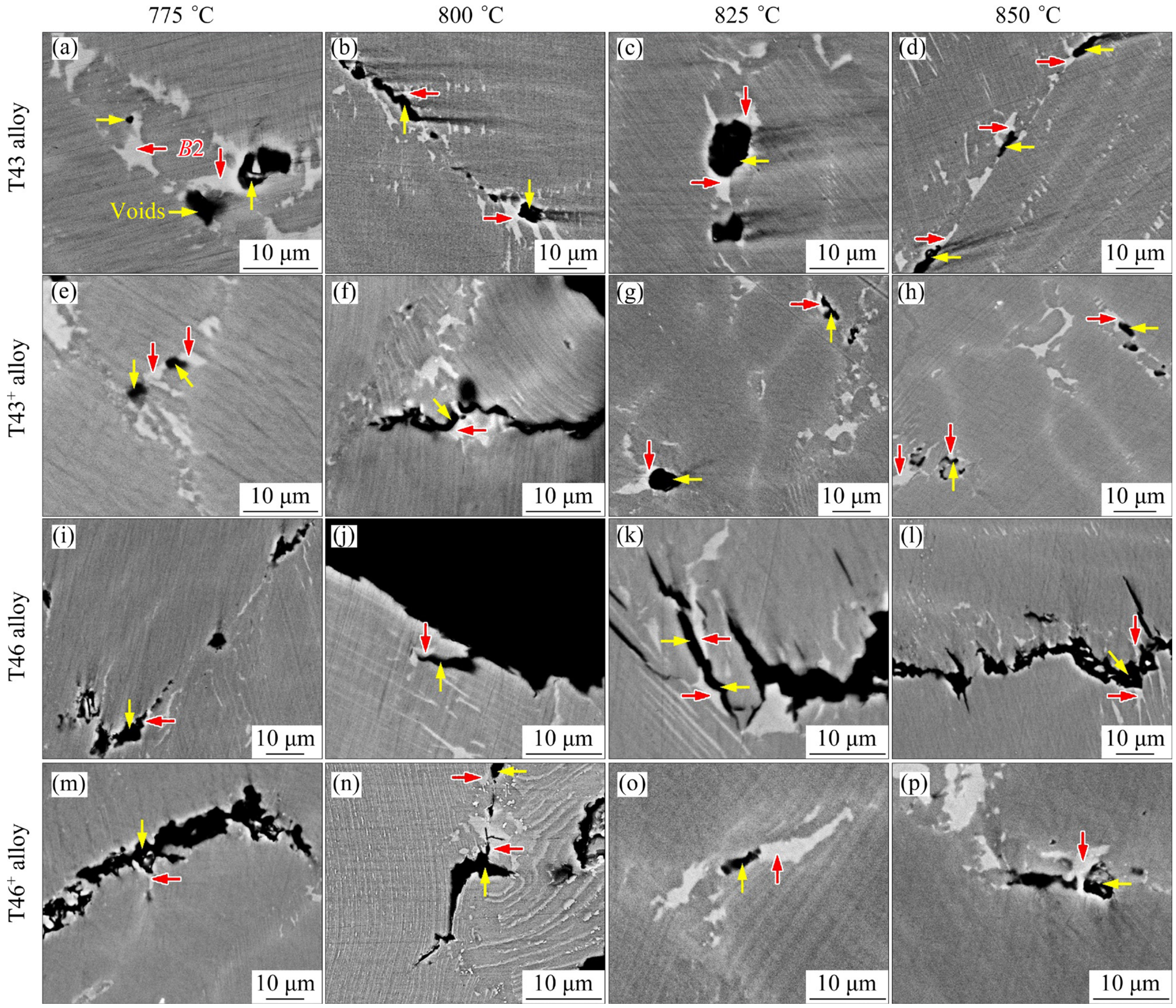

Fig. 7 Nucleation sites of voids and cracks of four investigated alloys during creep at different temperatures

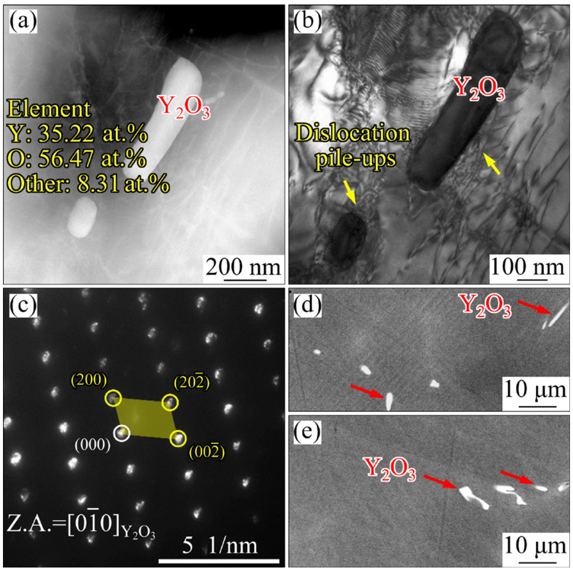

Fig. 8 Morphology of Y_2O_3 particles after creep: (a) HAADF image; (b) BF TEM image; (c) SAED pattern; (d, e) SEM images

particles are Y_2O_3. It can be clearly seen from the bright field (BF) TEM image in Fig. 8(b) that there are dislocation pile-ups at Y_2O_3/matrix interface, which manifests that Y_2O_3 particles have the ability to hinder dislocation slip. The dislocation pile-ups may generate local back stress in soft γ matrix, which can slow down the subsequent dislocation motion and result in creep deceleration. In addition, due to the strong bonding strength between Y_2O_3 and matrix, no cracks or voids appear at the Y_2O_3/matrix interface under the action of stress concentration caused by the dislocation pile-ups at the interface (Figs. 8(d, e)). This creates favorable conditions for Y_2O_3 particles to play a stable strengthening role.

3.4.2 Role of C/carbides

In TiAl alloys, the existence of element C mainly includes two forms, namely solid solution and precipitate as Ti$_x$AlC carbides. It can be seen from Fig. 1 that the element C mainly exists in the form of uniformly dispersed Ti$_2$AlC carbides in the lamellae in T46$^+$ alloy before creep, while it mainly exists in the form of dissolved C atoms in T43$^+$ alloy. In this study, the dynamic precipitation of carbides is found during creep of T43$^+$ alloy at 775 °C, as shown in Fig. 9. In the BF TEM image in Fig. 9(a), it can be clearly seen that fine ellipsoidal carbides precipitate in γ lamellae and there is a complex interaction between them and dislocations. From the HRTEM image in Fig. 9(b) and SAED patterns in Figs. 9(c−e), it can be inferred that these carbides are P-Ti$_3$AlC and maintain a well-established orientation relationship with the γ matrix as $(111)_{\mathrm{Ti_3AlC}}//(\bar{1}11)_\gamma$, and $[01\bar{1}]_{\mathrm{Ti_3AlC}}//[0\bar{1}1]_\gamma$. Subsequently, the geometric phase analysis (GPA) method was applied to evaluate the local strain distribution near Ti$_3$AlC carbides, where the HRTEM image in Fig. 9(b) was used as the input for the GPA calculation. The GPA results are shown in Fig. 9(f). According to the quantitative calculation results in Fig. 9(g), it can be found that Ti$_3$AlC carbides are mainly subjected to compressive strain. In addition, a special structure is generated at the interface between Ti$_3$AlC and matrix (Region R3 in Fig. 9(b)). As indicated by the yellow dotted line in Fig. 9(i), there are a series of extended straight lines perpendicular to the stacking fault plane among the diffraction spots, proving that this special structure is the stacking fault (SF). The method of identifying SF using this diffraction characteristic has been widely recognized [39]. In addition, from the superposition of GPA map and HRTEM image in Fig. 9(h), it can be found that the SFs exhibit a different strain distribution from the matrix, which means that the generation of SFs may hinder the dislocation motion. Similarly, QI et al [40] clarified that the SFs can inhibit more dislocation slips. During creep, with the precipitation of Ti$_3$AlC, misfit strain and lattice distortion energy are formed between Ti$_3$AlC and γ matrix, which provides the driving force for the generation of SFs. Meanwhile, Ti$_3$AlC carbides

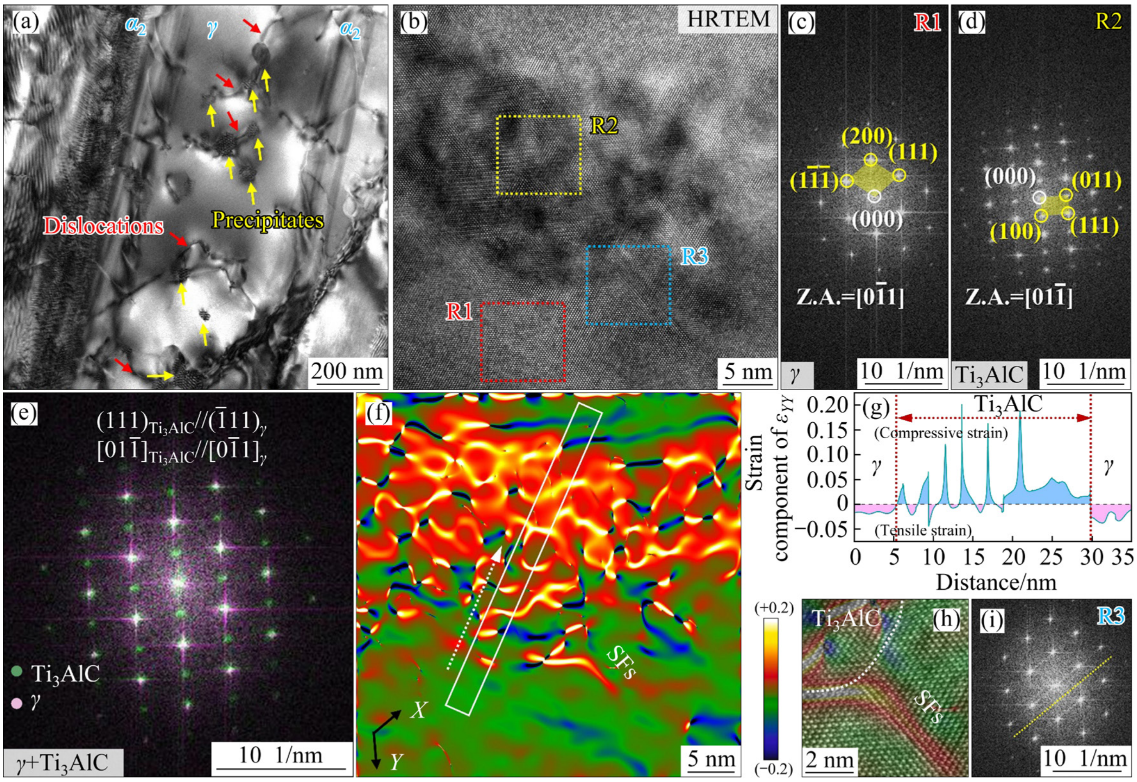

Fig. 9 Precipitation of carbide in T43$^+$ alloy during creep at 775 °C: (a) BF TEM image of precipitates in γ phase; (b) HRTEM image of precipitate and matrix; (c, d) SAED patterns obtained via fast Fourier transform (FFT) on Regions R1 and R2 marked in (b); (e) SAED pattern of precipitate and matrix obtained via FFT; (f) GPA map of strain distribution of entire region in (b) ($X//[111]_\gamma$ and $Y//[\bar{2}00]_\gamma$); (g) ε_{YY} strain partitioning curve of white rectangle region marked in (f) (The scanning direction is shown by white arrow); (h) Superposition of HRTEM image and GPA map of Region R3 in (b); (i) SAED pattern of γ matrix containing SFs obtained via FFT

have a complex reaction with dislocations, which is likely to induce the dissociation of perfect dislocation, resulting in partial dislocations. Then, the slip of partial dislocation leads to the formation of SFs [41].

In order to verify the universality of the dynamic precipitation of Ti_3AlC during creep, the microstructures of T43$^+$ and T46$^+$ alloys after creep at lower temperature (775 °C) and higher temperature (850 °C) were analyzed by TEM in detail, as shown in Fig. 10. For T43$^+$ alloy, fine dispersed Ti_3AlC carbides are found in γ lamellae at different positions at 775 °C (Figs. 10(a, b)). These carbides can effectively pin dislocations, thereby slowing down the creep rate. Surprisingly, numerous Ti_3AlC carbides also precipitate in γ lamellae at 850 °C (Fig. 10(c)). The average size increases from 41.7 nm at 775 °C to 67.4 nm at 850 °C, as shown in Fig. 11(a). These carbides can still effectively pin dislocations. In addition, the carbides precipitating at 850 °C can also induce the formation of SFs (Figs. 10(d, d_1)). From the above analyses, it can be deduced that in the creep process of T43$^+$ alloy at different temperatures, in addition to the strengthening caused by Y_2O_3 particles and dissolved C atoms, the dynamically precipitated Ti_3AlC carbides also play a key role.

For T46$^+$ alloy, after creep at 775 °C, a large number of Ti_3AlC carbides with an average size of 51.4 nm precipitate, and dislocations are pinned to form complex dislocation tangles (Fig. 10(e)). As the creep temperature increases to 850 °C, the average size of Ti_3AlC carbides increases to 112.6 nm, and carbides still exhibit a good ability to pin dislocations (Figs. 10(g) and 11(a)). It is worth noting that after creep of T46$^+$ alloy, not only new Ti_3AlC carbides precipitate, but also the initial Ti_2AlC particles still exist (Figs. 10(f, h)). On the one hand, the initial Ti_2AlC and the newly-formed Ti_3AlC exist in different locations. The initial Ti_2AlC particles mainly exist in α_2 lamellae, while the newly-formed Ti_3AlC mainly exists in γ phase. On the other hand, the average size of initial Ti_2AlC particles is much larger than that of newly-formed Ti_3AlC particles. The average size of Ti_2AlC particles is 357.5 nm after creep at 775 °C and 359.6 nm after creep at 850 °C, which is basically the same as that of 349.2 nm before creep. This also indicates that the Ti_2AlC particles can maintain good high-temperature stability during creep. The existence of Ti_2AlC particles is beneficial to improving the high-temperature stability of α_2/γ lamellar structure. Stable lamellar structure is one of the important factors for TiAl alloy to obtain high creep resistance [42]. Therefore, in T46$^+$ alloy, creep strengthening effect is mainly resulted from the dispersion strengthening of Y_2O_3 particles, precipitation hardening of dynamically precipitated Ti_3AlC particles as well as the stabilization of initial Ti_2AlC on the lamellae.

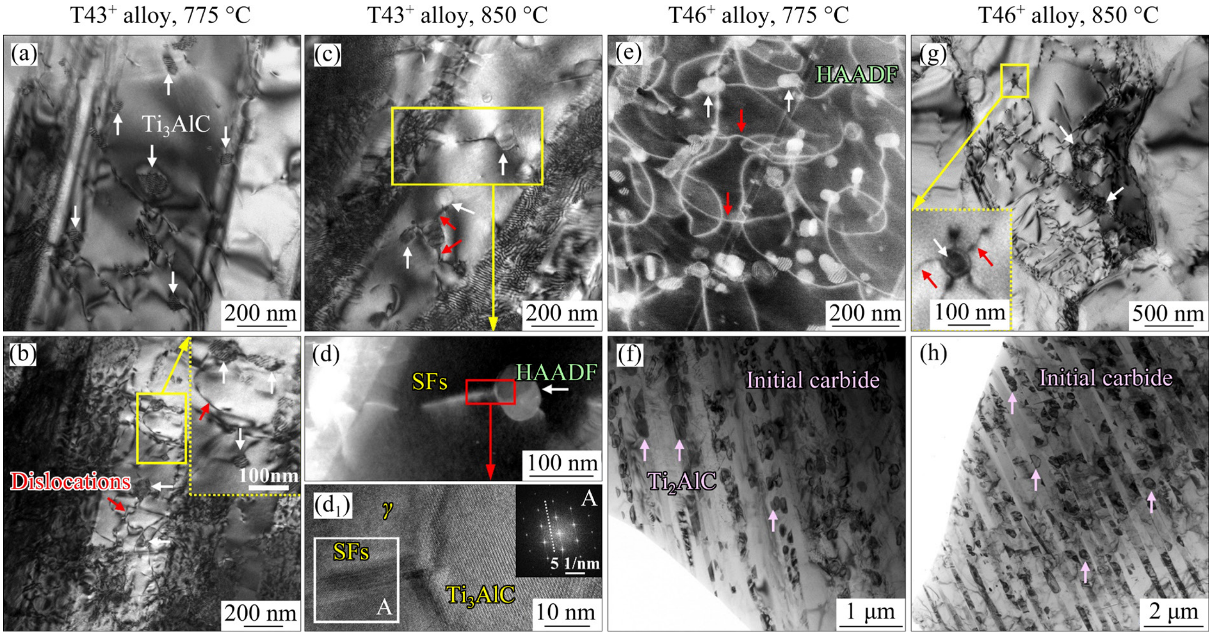

Fig. 10 Precipitation of carbides in T43$^+$ alloy and T46$^+$ alloy at 775 °C and 850 °C

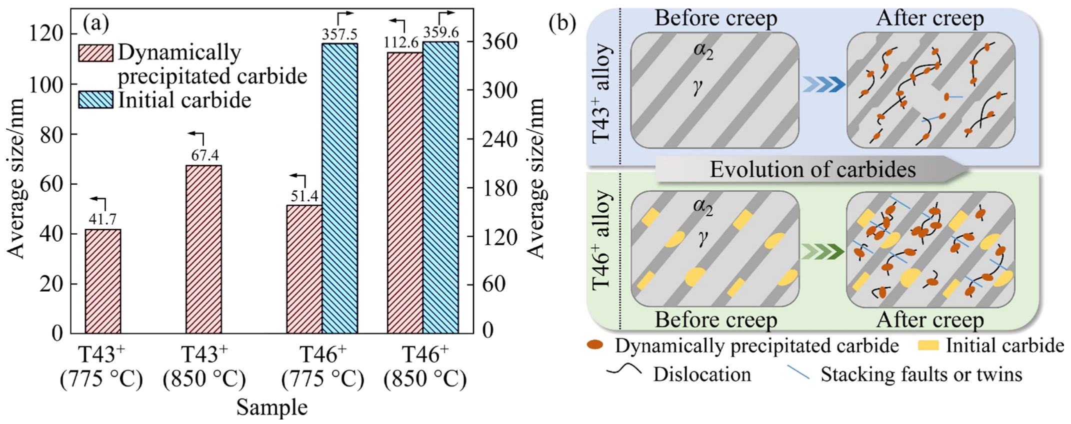

Fig. 11 Average size of carbides in T43$^+$ and T46$^+$ alloys at 775 and 850 °C (a); Schematic of carbide precipitation process (b)

Figure 11(b) illustrates the role of C/carbides in T43$^+$ and T46$^+$ alloys. For T43$^+$ alloy, C atoms are dissolved in the matrix, and no carbides are formed before creep. During creep, fine Ti_3AlC carbides precipitate and effectively pin dislocations. For T46$^+$ alloy, the C content exceeds the solid solubility limit, so Ti_2AlC particles are formed in the lamellae before creep. During creep, the presence of these Ti_2AlC particles can stabilize the lamellar structure and weaken lamellar degradation. Meanwhile, Ti_3AlC carbides also precipitate in T46$^+$ alloy, and the complex interaction with dislocations slows down the dislocation slip rate. Therefore, whether in T43$^+$ alloy or T46$^+$ alloy, the strengthening effect by element C is caused by many factors.

3.4.3 Role of nanotwins

The above analysis manifests that T46$^+$ alloy has higher creep resistance than T43$^+$ alloy. On the one hand, higher Al content is beneficial to the extension of creep life, which is verified by the creep data of T43 and T46 alloys in Fig. 2. This is mainly attributed to the decrease in the content of hard and brittle *B*2 phase in T46 alloy with higher Al content. According to the statistics at the beginning of Section 3.4, in the longer creep life of T46$^+$ alloy than T43$^+$ alloy, the strengthening amplitude caused by the increase of Al content accounts for half at most. Additionally, it is widely believed that the stabilizing effect of Ti_2AlC in T46$^+$ alloy on the lamellae is stronger than that of dissolved C atoms in T43$^+$ alloy, which is also responsible for the longer creep life of T46$^+$ alloy. More importantly, there is another special strengthening mechanism, namely twin strengthening. This novel strengthening concept is gradually applied to improving the tensile and compressive properties of TiAl alloys, and its feasibility and rationality are recognized [43,44].

Through detailed TEM observation, there is no twin in T43$^+$ alloy, but there are abundant twins in T46$^+$ alloy. As shown in Fig. 12(a), a large number of nanotwins are generated in T46$^+$ alloy after creep at 775 °C, which can be proved by the HRTEM image in Fig. 12(b) and the SAED pattern in Fig. 12(c). Besides, there are complex interactions between twins and dislocations. According to the GPA map and strain distribution curve in Figs. 12(d−f), it can be found that the twins and matrix exhibit completely different local strain fields, and the strain level at the twin boundary is the largest. Therefore, it is reasonable to speculate that twin boundaries/twins can act as obstacles to dislocation motion during creep. Then, the existence of twins and twin intersections can greatly shorten the mean free path for dislocation motion, thus enhancing the work hardening ability, so that the alloy can maintain a long steady-state creep stage. Meanwhile, with the dynamic precipitation of Ti_3AlC carbides, a more complex interaction among dislocations, twins and carbides gradually occurs (Fig. 12(g)), which further reduces the dislocation mobility. Similarly, after creep at 850 °C, there are still numerous twins in T46$^+$ alloy, and more abundant twin intersections are formed due to stronger thermal activation (Fig. 12(h)). Therefore, twin strengthening plays a key role in the high creep resistance of T46$^+$ alloy.

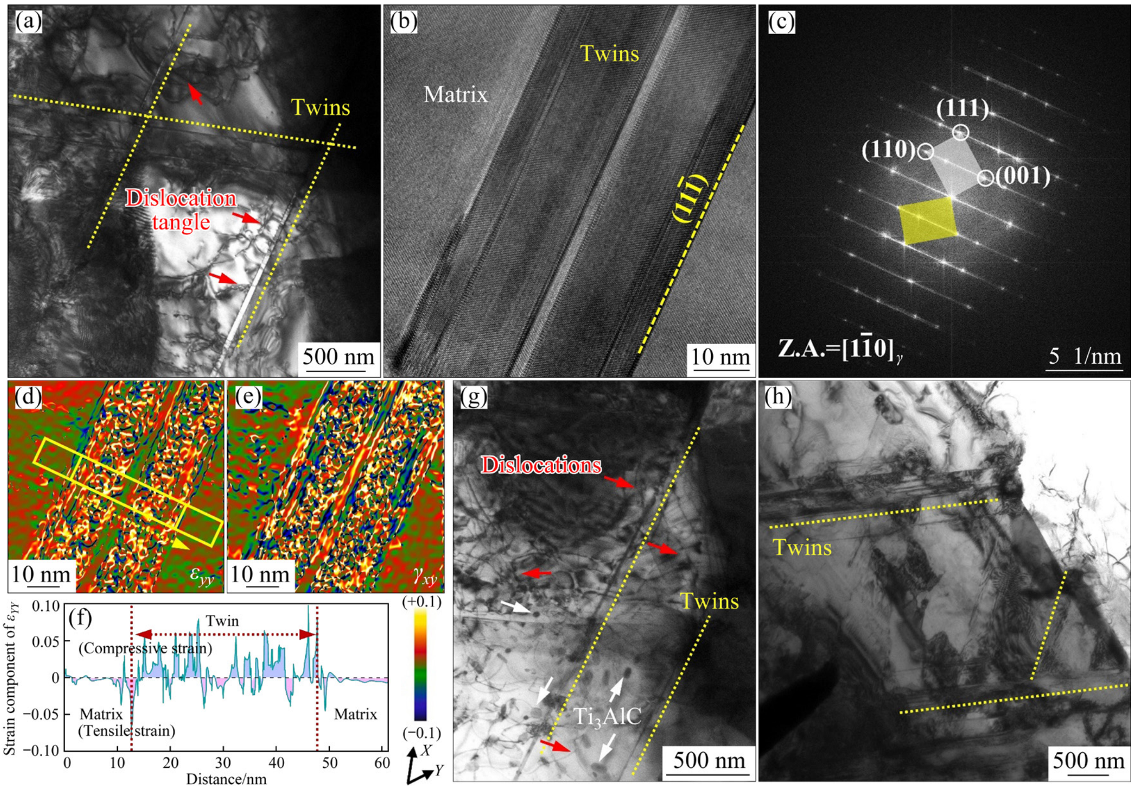

Fig. 12 Nanotwins in T46$^+$ alloy after creep at 775 °C (a−g) and 850 °C (h): (a) TEM image of interaction of twins and dislocations; (b) HRTEM image of twins; (c) SAED pattern obtained via FFT on entire region in (b); (d, e) GPA maps of strain distribution of entire region in (b) ($X//[111]_\gamma$ and $Y//[001]_\gamma$); (f) ε_{YY} strain partitioning curve of yellow rectangle region marked in (d) (The scanning direction is shown by yellow arrow); (g) TEM images of interaction among twins, dislocations and carbides; (h) TEM image of twin intersections

4 Conclusions

(1) Both the T43 and T46 alloys exhibit nearly lamellar structure, but the content of *B*2 phase in T46 alloy is lower than that in T43 alloy. By synergistic micro-alloying, Y_2O_3 particles are introduced into both alloys, while the C element exists in different forms. It exists as dissolved C atoms in low-Al alloy, but as Ti_2AlC particles in high-Al alloy. In addition, high-density nanotwins are induced in high-Al alloys.

(2) In the temperature range of 775−850 °C, the creep life of high-Al T46 alloy is about 58.08% longer than that of low-Al T43 alloy. By C/Y_2O_3 synergistic micro-alloying, the creep life of T43 and T46 alloys is obviously prolonged by an average of 237.85% and 379.43%, respectively. This composition design strategy has more significant advantages in improving creep performance of high-Al TiAl alloys.

(3) During creep at 775−850 °C, four alloys all fracture in mixed ductile−brittle mode. Creep voids tend to nucleate at the *B*2/*γ* phase interface and *B*2/lamellar colony boundary. The lamellar interface is strengthened by introducing C element, which results in a greater tendency to translamellar fracture. Meanwhile, the crack propagation resistance is also improved.

(4) There are multiple creep strengthening mechanisms induced by C/Y_2O_3 synergistic micro-alloying: dispersed Y_2O_3 particles can hinder dislocation slip; dynamically precipitated fine Ti_3AlC carbides can effectively pin dislocations; the dissolved C atoms and large-size Ti_2AlC particles can improve the lamellar stability. Particularly, the extra strengthening effect in high-Al alloys is attributed to high-density nanotwins.

CRediT authorship contribution statement

Zhen-quan LIANG: Writing − Original draft, Investigation, Software; **Shu-long XIAO:** Writing − Review & editing, Data curation, Conceptualization; **Ye TIAN:** Visualization, Software; **Yun-fei ZHENG:**

Methodology, Validation; **Ying-fei GUO:** Funding acquisition, Formal analysis; **Li-juan XU:** Supervision, Project administration, Conceptualization; **Xiang XUE:** Visualization, Data curation; **Jing TIAN:** Supervision, Resources.

Declaration of competing interest

The authors declare that they have no known competing financial interests or personal relationships that could have appeared to influence the work reported in this paper.

Acknowledgments

This work was supported by the National Natural Science Foundation of China (No. 52301138), and the National Defense Basic Scientific Research Project of China (No. 2019603018).

References

[1] CHEN Guang, PENG Ying-bo, ZHENG Gong, QI Zhi-xiang, WANG Min-zhi, YU Hui-chen, DONG Cheng-li, LIU C T. Polysynthetic twinned TiAl single crystals for high-temperature applications [J]. Nature Materials, 2016, 15: 876−881. https://doi.org/10.1038/nmat4677.

[2] SONG Lin, APPEL F, WANG Li, OEHRING M, HU Xing-guo, STARK A, HE Jun-yang, LORENZ U, ZHANG Tie-bang, LIN Jun-pin, PYCZAK F. New insights into high-temperature deformation and phase transformation mechanisms of lamellar structures in high Nb-containing TiAl alloys [J]. Acta Materialia, 2020, 186: 575−586. https://doi.org/10.1016/j.actamat.2020.01.021.

[3] LI Xiao-bing, XU Hao, XING Wei-wei, CHEN Bo, SHU Lei, ZHANG Meng-shu, LIU Kui. Microstructural evolution and mechanical properties of forged β-solidified γ-TiAl alloy by different heat treatments [J]. Transactions of Nonferrous Metals Society of China, 2022, 32: 2229−2242. https://doi.org/10.1016/S1003-6326(22)65943-0.

[4] ZHAO Peng-xiang, LI Xiao-bing, XING Wei-wei, CHEN Bo, MA Ying-che, LIU Kui. Cyclic oxidation behavior of Nb/Mn/Si alloying beta-gamma TiAl alloys [J]. Transactions of Nonferrous Metals Society of China, 2023, 33: 128−140. https://doi.org/10.1016/S1003-6326(22)66095-3.

[5] ISMAEEL A, WANG Cun-shan. Effect of Nb additions on microstructure and properties of γ-TiAl based alloys fabricated by selective laser melting [J]. Transactions of Nonferrous Metals Society of China, 2019, 29: 1007−1016. https://doi.org/10.1016/S1003-6326(19)65009-0.

[6] DUAN Bao-hua, YANG Yu-chen, HE Shi-yu, FENG Qi-sheng, MAO Lu, ZHANG Xue-xian, JIAO Li-na, LU Xiong-gang, CHEN Guang-yao, LI Chong-he. History and development of γ-TiAl alloys and the effect of alloying elements on their phase transformations [J]. Journal of Alloys and Compounds, 2022, 909: 164811. https://doi.org/10.1016/j.jallcom.2022.164811.

[7] HUANG Hai-tao, DING Hong-sheng, XU Xue-song, CHEN Rui-run, GUO Jing-jie, FU Heng-zhi. Phase transformation and microstructure evolution of a beta-solidified gamma-TiAl alloy [J]. Journal of Alloys and Compounds, 2021, 860: 158082. https://doi.org/10.1016/j.jallcom.2020.158082.

[8] XU Wen-chen, HUANG Kai, WU Shi-feng, ZONG Ying-ying, SHAN De-bin. Influence of Mo content on microstructure and mechanical properties of β-containing TiAl alloy [J]. Transactions of Nonferrous Metals Society of China, 2017, 27: 820−828. https://doi.org/10.1016/S1003-6326(17)60094-3.

[9] CHEN Rui-run, ZHAO Xiao-ye, YANG Yong, GUO Jing-jie, DING Hong-sheng, SU Yan-qing, FU Heng-zhi. Effect of Zr on microstructure and mechanical properties of binary TiAl alloys [J]. Transactions of Nonferrous Metals Society of China, 2018, 28: 1724−1734. https://doi.org/10.1016/S1003-6326(18)64816-2.

[10] YANG Yong, FENG He-ping, WANG Qi, CHEN Rui-run, GUO Jing-jie, DING Hong-sheng, SU Yan-qing. Improvement of microstructure and mechanical properties of TiAl−Nb alloy by adding Fe element [J]. Transactions of Nonferrous Metals Society of China, 2020, 30: 1315−1324. https://doi.org/10.1016/S1003-6326(20)65298-0.

[11] JIA Yi, LIU Zhi-dong, LI Sha, YAO Hao-ming, REN Zhong-kai, WANG Tao, HAN Jian-chao, XIAO Shu-long, CHEN Yu-yong. Effect of cooling rate on solidification microstructure and mechanical properties of TiB_2-containing TiAl alloy [J]. Transactions of Nonferrous Metals Society of China, 2021, 31: 391−403. https://doi.org/10.1016/S1003-6326(21)65504-8.

[12] ZHOU Can-xu, LIU Bin, LIU Yong, QIU Cong-zhang, LI Hui-zhong, HE Yue-hui. Effect of carbon on high temperature compressive and creep properties of β-stabilized TiAl alloy [J]. Transactions of Nonferrous Metals Society of China, 2017, 27: 2400−2405. https://doi.org/10.1016/S1003-6326(17)60266-8.

[13] KIM J H, KIM S W, LEE H N, OH M H, INUI H, WEE D M. Effects of Si and C additions on the thermal stability of directionally solidified TiAl−Nb alloys [J]. Intermetallics, 2005, 13: 1038−1047. https://doi.org/10.1016/j.intermet.2004.10.010.

[14] ZHANG Tie-bang, WU Ze-en, HU Rui, ZHANG Fan, KOU Hong-chao, LI Jin-shan. Influence of nitrogen on the microstructure and solidification behavior of high Nb containing TiAl alloys [J]. Materials & Design, 2016, 103: 100−105. https://doi.org/10.1016/j.matdes.2016.04.071.

[15] LIU Z G, CHAI L H, CHEN Y Y. Effect of cooling rate and Y element on the microstructure of rapidly solidified TiAl alloys [J]. Journal of Alloys and Compounds, 2010, 504: S491−S495. https://doi.org/10.1016/j.jallcom.2010.02.054.

[16] TAN Ying-mei, FANG Hong-ze, CHEN Rui-run, LIU Yang-li, SU Yan-qing, GUO Jing-jie, CUI Hong-zhi, ZHANG Shu-yan, FU Heng-zhi. Microalloying effects of Ho on microstructure evolution and high temperature properties of Ti46Al4Nb1Mo alloy [J]. Intermetallics, 2020, 126: 106883. https://doi.org/10.1016/j.intermet.2020.106883.

[17] PANIN P V, KOCHETKOV A S, ZAVODOV A V, LUKINA E A. Effect of Gd addition on phase composition, structure, and properties of beta-solidifying TiAl-based alloy with Zr

and Cr content variability [J]. Intermetallics, 2020, 121: 106781. https://doi.org/10.1016/j.intermet.2020.106781.

[18] HADI M, MERATIAN M, SHAFYEI A. The effect of lanthanum on the microstructure and high temperature mechanical properties of a beta-solidifying TiAl alloy [J]. Journal of Alloys and Compounds, 2015, 618: 27−32. https://doi.org/10.1016/j.jallcom.2014.08.124.

[19] SCHEU C, STERGAR E, SCHOBER M, CHA L, CLEMENS H, BARTELS A, SCHIMANSKY F P, CEREZO A. High carbon solubility in a γ-TiAl-based Ti−45Al−5Nb−0.5C alloy and its effect on hardening [J]. Acta Materialia, 2009, 57: 1504−1511. https://doi.org/10.1016/j.actamat.2008.11.037.

[20] FANG Hong-ze, CHEN Rui-run, YANG Yong, SU Yan-qing, DING Hong-sheng, GUO Jing-jie, FU Heng-zhi. Role of graphite on microstructural evolution and mechanical properties of ternary TiAl alloy prepared by arc melting method [J]. Materials & Design, 2018, 156: 300−310. https://doi.org/10.1016/j.matdes.2018.06.048.

[21] SONG Lin, HU Xing-guo, WANG Li, STARK A, LAZURENKO D, LORENZ U, LIN Jun-pin, PYCZAK F, ZHANG Tie-bang. Microstructure evolution and enhanced creep property of a high Nb containing TiAl alloy with carbon addition [J]. Journal of Alloys and Compounds, 2019, 807: 151649. https://doi.org/10.1016/j.jallcom.2019.151649.

[22] LI Ming-ao, XIAO Shu-long, XU Li-juan, TIAN Jing, CHEN Yu-yong. Microscale investigation of perovskite-Ti_3AlC strengthening and plastic deformation in high niobium containing TiAl alloys [J]. Journal of Alloys and Compounds, 2021, 857: 157563. https://doi.org/10.1016/j.jallcom.2020.157563.

[23] CUI Sen, CUI Chun-xiang, YANG Shi-chao, LIU Shuang-jin. Microstructure and mechanical properties of hybrid in-situ Ti_2AlC_w/Mo_2B_{5p} reinforced TiAl alloy [J]. Materials Science and Engineering A, 2022, 829: 142182. https://doi.org/10.1016/j.msea.2021.142182.

[24] YANG Shi-chao, CUI Chun-xiang, CUI Sen, LIU Shuang-jin. Ti−46Al−4Nb alloy refined and reinforced by in-situ TiC nanoparticles and TiB_2 whiskers [J]. Journal of Alloys and Compounds, 2022, 892: 162195. https://doi.org/10.1016/j.jallcom.2021.162195.

[25] CUI Sen, CUI Chun-xiang, YANG Shi-chao, KANG Li-cong. The effect of the in-situ hybrid Ti_5Si_{3p}/Ti_2AlN_w on the microstructure and mechanical properties of TiAl [J]. Materials Letters, 2021, 304: 130678. https://doi.org/10.1016/j.matlet.2021.130678.

[26] WANG Qi, CHEN Rui-run, YANG Yao-hua, GUO Jing-jie, SU Yan-qing, DING Hong-sheng, FU Heng-zhi. Effects of V and B, Y additions on the microstructure and creep behaviour of high-Nb TiAl alloys [J]. Journal of Alloys and Compounds, 2018, 747: 640−647. https://doi.org/10.1016/j.jallcom.2018.03.055.

[27] GUO Ying-fei, TIAN Jing, XIAO Shu-long, XU Li-juan, CHEN Yu-yong. Elevated temperature performance and creep behavior of Y_2O_3 reinforced Ti−48Al−6Nb alloy at the brittle-ductile transition temperature [J]. Journal of Alloys and Compounds, 2021, 871: 159497. https://doi.org/10.1016/j.jallcom.2021.159497.

[28] LIANG Zhen-quan, XIAO Shu-long, SHAO Yi, CHI Da-zhao, LI Xin-yi, ZHENG Yun-fei, XU Li-juan, XUE Xiang, TIAN Jing, CHEN Yu-yong. Effects of tailoring microstructure on short-term creep behavior of high Nb containing TiAl alloys under various stress levels [J]. Journal of Materials Research and Technology, 2023, 25: 532−545. https://doi.org/10.1016/j.jmrt.2023.05.231.

[29] APPEL F, PAUL J D H, OEHRING M, FRÖBEL U, LORENZ U. Creep behavior of TiAl alloys with enhanced high-temperature capability [J]. Metallurgical and Materials Transactions A, 2003, 34: 2149−2164. https://doi.org/10.1007/s11661-003-0279-6.

[30] LIANG Zhen-quan, XIAO Shu-long, CHI Da-zhao, ZHENG Yun-fei, XU Li-juan, XUE Xiang, TIAN Jing, CHEN Yu-yong. Compressive creep behavior of high Nb containing TiAl alloy: Dynamic recrystallization and phase transformation [J]. Intermetallics, 2023, 163: 108067. https://doi.org/10.1016/j.intermet.2023.108067.

[31] MISHIN Y, HERZIG C. Diffusion in the Ti−Al system [J]. Acta Materialia, 2000, 48: 589−623. https://doi.org/10.1016/S1359-6454(99)00400-0.

[32] HERZIG C, PRZEORSKI T, MISHIN Y. Self-diffusion in γ-TiAl: An experimental study and atomistic calculations [J]. Intermetallics, 1999, 7: 389−404. https://doi.org/10.1016/S0966-9795(98)00117-4.

[33] SINGH V, MONDAL C, SARKAR R, BHATTACHARJEE P P, GHOSAL P. Compressive creep behavior of a γ-TiAl based Ti−45Al−8Nb−2Cr−0.2B alloy: The role of β(B2)-phase and concurrent phase transformations [J]. Materials Science and Engineering: A, 2020, 774: 138891. https://doi.org/10.1016/j.msea.2019.138891.

[34] WANG Qi, CHEN Rui-run, CHEN De-zhi, SU Yan-qing, DING Hong-sheng, GUO Jing-jie, FU Heng-zhi. The characteristics and mechanisms of creep brittle-ductile transition in TiAl alloys [J]. Materials Science and Engineering A, 2019, 767: 138393. https://doi.org/10.1016/j.msea.2019.138393.

[35] CABIBBO M. Carbon content driven high temperature γ−α_2 interface modifications and stability in Ti−46Al−4Nb intermetallic alloy [J]. Intermetallics, 2020, 119: 106718. https://doi.org/10.1016/j.intermet.2020.106718.

[36] CHAN K S, WANG P, BHATE N, KUMAR K S. Intrinsic and extrinsic fracture resistance in lamellar TiAl alloys [J]. Acta Materialia, 2004, 52: 4601−4614. https://doi.org/10.1016/j.actamat.2004.06.026.

[37] GUO Ying-fei, CHEN Yu-yong, XIAO Shu-long, TIAN Jing, ZHENG Zhuang-zhuang, XU Li-juan. Influence of nano-Y_2O_3 addition on microstructure and tensile properties of high-Al TiAl alloys [J]. Materials Science and Engineering A, 2020, 794: 139803. https://doi.org/10.1016/j.msea.2020.139803.

[38] YUE Hang-yu, PENG Hui, MIAO Ke-song, GAO Bo-yang, WU Hao, YANG Ji-bang, FAN Guo-hua. Significant enhancement in high-temperature tensile strength of trace nano-Y_2O_3-reinforced TiAl alloy prepared by selective electron beam melting [J]. Materials Science and Engineering A, 2023, 875: 145086. https://doi.org/10.1016/j.msea.2023.145086.

[39] ZHENG Guo-ming, TANG Bin, ZHAO Song-kuan, WANG Jun, XIE Yi-zhen, CHEN Xiao-fei, WANG W Y, LIU Dong,

YANG Rui, LI Jin-shan. Breaking the high-temperature strength-ductility trade-off in TiAl alloys through microstructural optimization [J]. International Journal of Plasticity, 2023, 170: 103756. https://doi.org/10.1016/j.ijplas.2023.103756.

[40] QI Wu, YANG Xiao, WANG Wen-rui, PENG Tao, ZHANG Ya, LI Yong, ZHANG Yong. Effects of Ta microalloying on the microstructure and mechanical properties of $L1_2$-strengthened CoCrFeNi−AlTi high-entropy alloys [J]. Materials Science and Engineering A, 2023, 875: 145048. https://doi.org/10.1016/j.msea.2023.145048.

[41] ZHENG Guo-ming, TANG Bin, ZHAO Song-kuan, WANG W Y, CHEN Xiao-fei, ZHU Lei, LI Jin-shan. Evading the strength-ductility trade-off at room temperature and achieving ultrahigh plasticity at 800 °C in a TiAl alloy [J]. Acta Materialia, 2022, 225: 117585. https://doi.org/10.1016/j.actamat.2021.117585.

[42] LIU Yan, TANG Bin, HUANG Xiao-yu, ZHU Lei, LIU Dong, YANG Rui, LI Jin-shan. Microstructural stability and creep properties of middle Nb γ-TiAl alloy with a modulated microstructure [J]. Intermetallics, 2022, 151: 107733. https://doi.org/10.1016/j.intermet.2022.107733.

[43] LIU Shi-qiu, DING Hong-sheng, CHEN Rui-run, GUO Jing-jie, FU Heng-zhi. Remarkable improvement in tensile strength of a polycrystalline γ-TiAl-based intermetallic alloy by deformation nanotwins [J]. Materials Science and Engineering A, 2021, 823: 141692. https://doi.org/10.1016/j.msea.2021.141692.

[44] LIU Shi-qiu, DING Hong-sheng, ZHANG Hai-long, CHEN Rui-run, GUO Jing-jie, FU Heng-zhi. High-density deformation nanotwin induced significant improvement in the plasticity of polycrystalline γ-TiAl-based intermetallic alloys [J]. Nanoscale, 2018, 10: 11365−11374. https://doi.org/10.1039/C8NR01659C.

C 和 Y_2O_3 协同微合金化 TiAl 合金在不同温度下的蠕变行为和显微组织演变

梁振泉 [1,2]，肖树龙 [1,2]，田 野 [1,2]，郑云飞 [1,2]，郭应飞 [3]，徐丽娟 [1,2]，薛 祥 [1,2]，田 竞 [1,2]

1. 哈尔滨工业大学 金属精密热加工国家级重点实验室，哈尔滨 150001；
2. 哈尔滨工业大学 材料科学与工程学院，哈尔滨 150001；
3. 贵州大学 材料与冶金学院，贵阳 550025

摘　要：采用先进电子显微技术研究了感应凝壳熔炼(ISM)制备的 C/Y_2O_3 协同微合金化高铝和低铝 TiAl 合金的显微组织和蠕变行为。显微组织分析表明：Y_2O_3 颗粒弥散分布在两类 TiAl 合金中；元素 C 以固溶形式存在于低铝合金中，而以 Ti_2AlC 颗粒形式存在于高铝合金片层中。此外，高铝 TiAl 合金中产生高密度纳米孪晶。蠕变数据证实 C/Y_2O_3 微合金化显著强化 TiAl 合金的蠕变抗力，这得益于 Y_2O_3 颗粒的弥散强化、动态析出的 Ti_3AlC 颗粒的沉淀强化以及固溶 C 原子或 Ti_2AlC 颗粒造成的片层稳定化。此策略对于高铝 TiAl 合金的蠕变抗力有更显著的提升作用，这归因于额外的孪晶强化效应。在 775~850 ℃范围内，这些合金以韧脆混合模式发生蠕变断裂，但随着温度的升高，断裂特征有所改变。

关键词：微合金化 TiAl 合金；蠕变行为；孪晶强化；碳化物析出；断裂特征

(Edited by Bing YANG)